AIAA JOURNAL
Vol. 32, No. 5, May 1994

Numerical Study of Transient Flow Phenomena in Shock Tunnels

Susan Tokarcik-Polsky* and Jean-Luc Cambier†
Eloret Institute, Palo Alto, California 94303

Computational fluid dynamics (CFD) was used to study some transient flow features that can occur during the startup process of a shock tunnel. The investigation concentrated on two areas: 1) the flow near the endwall of the driven tube during shock reflection and 2) the transient flow in the nozzle. The driven tube calculations were inviscid and focused on the study of a vortex system that was seen to form at the driven tube's axis of symmetry. The nozzle flow calculations examined viscous and inviscid effects during nozzle startup. The CFD solutions of the nozzle flows were compared with experimental data to demonstrate the effectiveness of the numerical analysis.

Nomenclature

A = area (*throat area)
h = height
$i0, i1$ = grid cell indices
M_s = Mach number of shock wave
N = number of species
Nn = number of points in i direction of grid n
p = pressure, Pa
r = radius
t = time, s
T = temperature, K
V = velocity, m/s
X_i = mole fraction of species i
x = axial coordinate (i) direction
y = radial coordinate (j) direction
Δ = change in
ρ, ρ_1 = density, freestream density, kg/m^3

Introduction

THIS work had two main objectives. The first and foremost was to study some of the transient starting processes that occur in shock tunnels. The initial, unsteady flow in a shock tunnel is important because it can affect the quality and duration of the resulting test flow. Because the starting flow is difficult to examine experimentally, computational fluid dynamics (CFD) was used to simulate the startup process. This leads to the second objective of this work, which was to evaluate the effectiveness of the time-accurate CFD analysis. This was accomplished by comparing the CFD results with experimental data, when they were available, for the particular problem that was computed. When experimental data particular to a specific problem were not available, a comparison was made with experimental data for a flowfield that had as many similarities as possible to the problem being explored.

A basic schematic of a shock tunnel is shown in Fig. 1. The shock tunnel consists of a driver tube filled with a light combustible mixture, a driven tube filled with the test gas at a low pressure, a supersonic nozzle evacuated to low pressure, and finally a test section. The gas in the driver tube is burned to produce a high-pressure and high-temperature gas. When the pressure is high enough, the primary diaphragm breaks and sends a planar shock wave down the driven tube. This shock wave partially reflects off the endwall of the driven tube and breaks the secondary diaphragm, sending flow through the nozzle. The gas in the driven tube behind the reflected shock wave forms the reservoir of high-pressure, high-temperature gas for the nozzle flow. Once the flow is steady at the nozzle exit, tests can be performed until the nozzle flow becomes contaminated with the driver gas. For more information on shock tunnel operations, see Ref. 1.

This work concentrated on only certain aspects of the entire starting process. The first area dealt with the vortex system formed during the shock reflection at the endwall of the driven tube. Several aspects of this transient flow were examined: 1) the effects of the numerical method, 2) the effects of geometric configuration, 3) the effects of time (how the flowfield changed as the reflected shock and vortex structure continued to propagate up the driven tube), and 4) the effects of axisymmetric and two-dimensional formulations. The vortex formation was essentially an inviscid phenomenon; therefore, viscous effects were not considered in this part of the study.

The second area dealt with the initial flow in the nozzle. The important features in this flowfield which were studied included 1) viscous effects (shock-wave/boundary-layer interactions, 2) resolution of contact discontinuities, and 3) accurate determination of general flow features such as shock speeds.

Numerical Method

The computations presented in this paper were performed using the code "MOZART" developed at NASA Ames Research Center by J.-L. Cambier. The code uses a finite volume, second-order total variation diminishing (TVD) scheme for the solution of the Euler equations. The scheme is similar to the original one of Harten,[2] extended to multiple species. Although the solver is capable of handling nonequilibrium chemical reactions, only nonreacting cases were considered here. The algorithm is directionally split. The viscous terms in the Navier-Stokes equations are solved by a second-order, centered, implicit scheme, which is also directionally split. Unsteady viscous calculations can then be performed efficiently without constraints on the time step imposed by viscous fluxes in regions of high shear. The implicit scheme for the viscous terms involves only the inversion of 3×3 matrices (in two dimensions). The Euler equations are solved explicitly, thus avoiding the need to invert large $(N + 3)^2$ matrices. When required, the chemistry is solved point implicitly.

The code uses multiple grids to handle complex geometries and to enhance resolution. The grids can be patched together at their boundaries or superimposed on top of one another. One particular feature that was used extensively in some of the calculations was

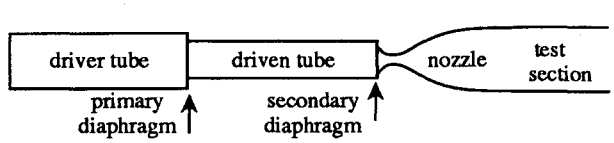

Fig. 1 Schematic of a typical shock tunnel facility.

Presented as Paper 93-2018 at the AIAA/SAE/ASME/ASEE 29th Joint Propulsion Conference, Monterey, CA, June 28–30, 1993; received July 23, 1993; revision received Dec. 20, 1993; accepted for publication Dec. 21, 1993. This paper is declared a work of the U.S. Government and is not subject to copyright protection in the United States.

*Research Scientist, MS 230-2, NASA Ames Research Center, Moffett Field, CA 94035. Member AIAA.

†Senior Research Scientist, MS 230-2, NASA Ames Research Center, Moffett Field, CA 94035. Member AIAA.

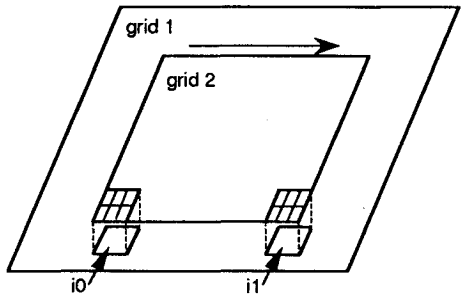

Fig. 2 Grid subdivision technique used to obtain high resolution in areas of interest. Grid 2 can move within grid 1 to track transient features.

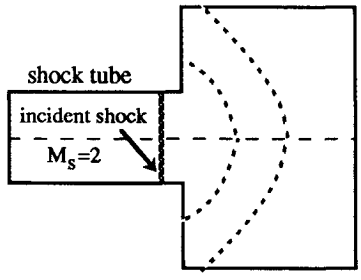

Fig. 3 Schematic of the shock tube experiment conducted by Mandella and Bershader.

the use of sliding grids. In this method, a coarse grid is established as a "background" grid, which generally encompasses most of the domain of study. Another grid of higher resolution is then established as a subset of the background grid. This new grid is set up such that the high-resolution cells form an exact subdivision of the background cells; for example, each background cell may contain three columns of high-resolution cells in one direction and two rows of high-resolution cells in the other. Thus, the change in resolution can be different for each direction. Since the scheme is finite volume, the values inside the background cells can be easily obtained as volume averages of the high-resolution cells.

The high-resolution grid is then allowed to move on top of the background grid, by elementary steps, such that the background cell is always subdivided into the same number of high-resolution cells (there is no fractional subdivision allowed). In this way the grid moves only occasionally, not necessarily at every time step. The mapping between the low- and high-resolution grids is always preserved. The motion of the grid results in a shift of indices in the mapping procedure. The previous example assumed a 3 to 1 subdivision scale in the i direction and a 2 to 1 subdivision in the j direction. Suppose that, initially, the cells ($i0$) to ($i1$) of the background grid (grid 1) in the i direction were subdivided and mapped into the cells (1) to ($N2$) of the higher resolution grid (grid 2). By definition, there are three times more cells in the i direction of grid 2 than in grid 1: $N2 = 3 \cdot (i1 - i0 + 1)$. The mapping is shown schematically in Fig. 2.

If grid 2 moves in the positive direction, the new mapping will be as follows: cells ($i0 + 1$) to ($i1 + 1$) will be subdivided into the $N2$ high-resolution cells. As grid 2 moves, cell ($i0$) of grid 1 ceases to be subdivided, and cell ($i1 + 1$) becomes subdivided. During this step, the variables for the high-resolution cells inside ($i1 + 1$) take the same values of the variables present in cell ($i1 + 1$).

The procedure can be repeated one step further by laying another high-resolution grid on top of grid 2. This procedure is an attempt to achieve high spatial resolution in regions of interest when these regions are in motion. It has the advantage of being very fast. Since the grid slides by steps of the background cell distance only, the mapping between the background and high-resolution grid is always the same, except for a shift of indices. The variable arrays can then simply be copied over with the shift of indices, without requiring interpolation or extrapolations. This technique was used for some of the calculations presented here and has been employed previously to calculate similar transient flows.[3]

Reflected Shock Simulation

The first area that was examined was the flow dynamics occurring during the shock reflection at the endwall of the driven tube. Recent numerical studies[3,4] predicted that the flow in this region was quite complex. A particularly important feature that was observed was a vortex system that formed at the axis of the driven tube. The vortex system caused the reflected shock to bulge out at the center. This bulging effect could potentially cause the reservoir gas to become contaminated with driver gas sooner than would be expected if the reflected shock was planar.

Vortical Flow Test Case

As mentioned earlier, the CFD results were compared with experimental data whenever they were available. However, for this particular case, whereas two-dimensional data exist, no data for this type of reflection in an axisymmetric situation exist. Therefore, an experiment that incorporated the major flow features of interest, in this case transient, vortical flow, was chosen to evaluate the effectiveness of the CFD analysis.

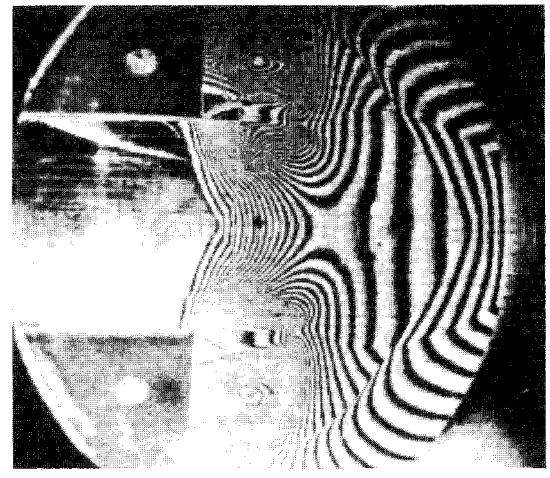

Fig. 4a Experimental interferogram of the flowfield at the exit of a shock tube.

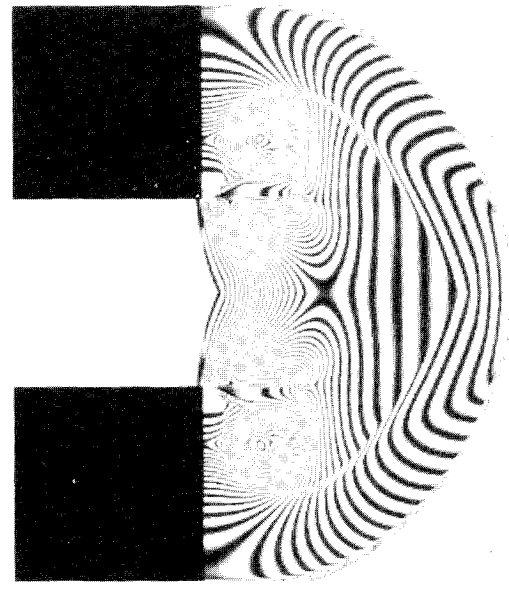

Fig. 4b Interferogram constructed from the computational flowfield at the exit of a shock tube.

The experiment was conducted by Mandella and Bershader[5,6] and consisted of a shock tube with a 5-cm × 5-cm cross section that generated a planar shock with $M_s = 2$ that expanded into a test section. The end of the shock tube was open to ambient conditions. Two parallel Plexiglas plates were attached to the end of the shock tube to keep the shock wave and the rest of the flowfield planar. A schematic of the experiment is shown in Fig. 3.

The planar shock wave started to diffract as soon as it left the shock tube, forming a curved shock wave. The experimental interferogram (Fig. 4a) shows that, as the shock wave propagated into the test section, vortices were formed in the vicinity of each of the 90-deg expansion corners. The contact surface, slipstream, and Prandtl-Meyer fan (which interacts with the vortices) can also be seen in the interferogram.

For the computational solutions, the flow was assumed to be inviscid with no chemical reactions. There were two grids patched together: one for the shock tube (125 × 80) and one for the test chamber (525 × 200). Grid tracking was not used for this case. A computed interferogram at approximately the same time as the experimental interferogram is shown in Fig. 4b. A comparison of the two figures demonstrates that the computations were able to predict all of the major flow features mentioned earlier, including the two vortices, with good accuracy. The synthetic interferogram was constructed with software developed at NASA Ames Research Center.[7]

Setup for Reflected Shock Simulation

The geometry for this problem was essentially that for the NASA Ames 16-in. shock tunnel. The driven tube radius was 6 in., the radius of the aperture at the end of the driven tube was 2.125 in., and the nominal radius of the throat was 1.625 in. The CFD calculations were started from the moment the primary shock reached the endwall of the driven tube and began to reflect. It was assumed that the secondary diaphragm broke ideally at this moment. All times given in this paper were measured assuming $t = 0$ s at this point. The initial conditions in the driven tube were as follows: $p = 50.76$ atm, $T = 3674$ K, $V = 2710$ m/s, $X_N = 0.6042 \times 10^{-4}$, $X_O = 0.04091$, $X_{N_2} = 0.7341$, $X_{O_2} = 0.1456$, and $X_{NO} = 0.07934$ (equilibrium composition). The initial conditions in the nozzle were $p = 1.3 \times 10^{-4}$ atm, $T = 298$ K, $V = 0.0$ m/s, $X_{N_2} = 0.79$, and $X_{O_2} = 0.21$. For the numerical analysis, the flow was assumed to be inviscid and chemically frozen.

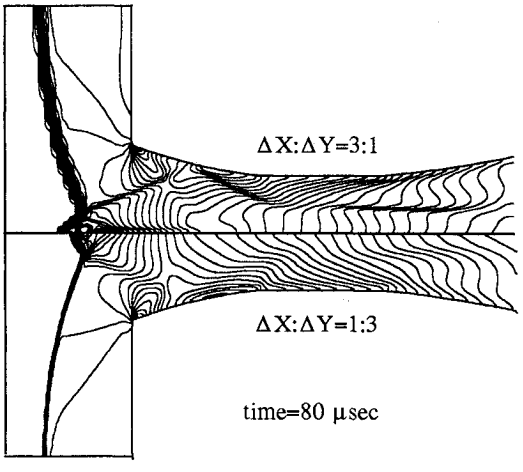

Fig. 5 Temperature contours show a jetting effect at the shock tunnel centerline (top). The jetting is relieved by choosing the proper grid aspect ratio near the axis (bottom).

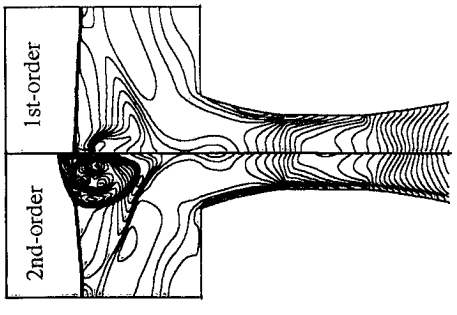

Fig. 6 A solution computed with first-order spatial accuracy (top) is compared to a solution computed with second-order spatial accuracy (bottom).

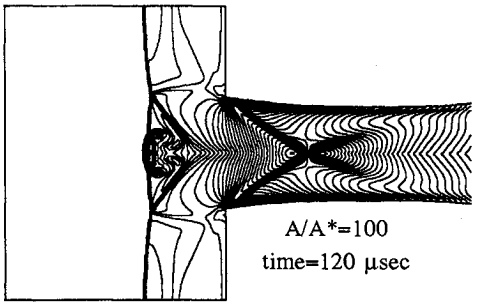

Fig. 7a Transient flowfield for a large throat size (temperature contours).

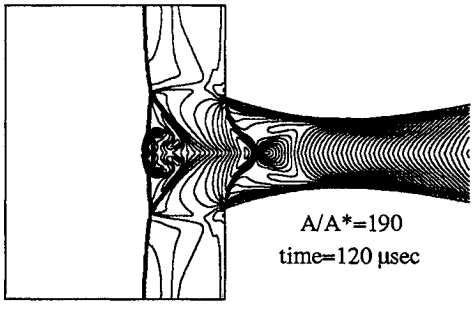

Fig. 7b Transient flowfield for a medium throat size (temperature contours).

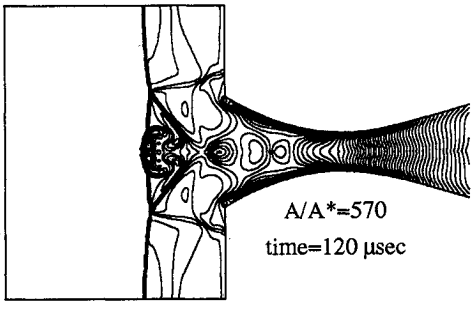

Fig. 7c Transient flowfield for a small throat size (temperature contours).

Results of Reflected Shock Simulation

Numerical Effects

Two components of the numerical technique were examined: 1) grid effects and 2) first-order vs second-order spatial accuracy. The grids used for this part of the study consisted of two patches: one for the driven tube (typically 231 × 91) and one for the nozzle section (typically 251 × 31). Grid influences were most critical at the axis of symmetry where the vortex system was formed. It was found that a solution computed on a grid where the cells near the axis had $\Delta x{:}\Delta y \geq 1$ (long and slender cells) showed a jetting phenomenon at the axis of symmetry. The jet diminished with radial distance away from the axis. The result of the jetting was that the bulge in the reflected shock formed a conical shape (i.e., <) around the axis of symmetry (top half of Fig. 5). Although shock interac-

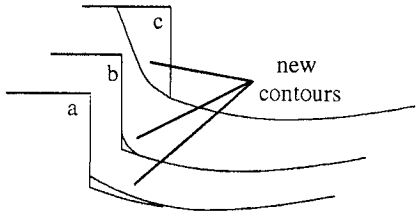

Fig. 8 Geometric changes made at the driven tube/nozzle interface.

tions can produce jets, a result such as this in a CFD solution, especially when it is near a singular axis, is cause to doubt whether a cone-shaped reflected shock is a physically realistic result. The jetting effect has been observed previously by Cambier et al.[3] and can also be seen in the results of Jacobs.[4] One explanation of this phenomenon, which was described in Ref. 3, is that the jetting was caused by the numerical representation of the singular axis in the axisymmetric formulation. It was assumed in Ref. 3 that the problem arose from the axisymmetric pressure correction term, which is not part of the monotonic (TVD) fluxes and acts as a nonconservative momentum source that behaves as $1/(\Delta r)$ near the axis. Therefore, clustering points near the axis [thus accentuating the $1/(\Delta r)$ term] aggravated the jetting.

It was suggested in Ref. 3 that coarsening the grid in the radial direction would alleviate the jetting problem. The bottom half of Fig. 5 shows the same case as computed on the top half; however, the grid aspect ratio was changed so that $\Delta x{:}\Delta y = 1{:}3$ (near the axis). Comparing the two solutions indicated that the nonphysical jetting effect was eliminated by the proper choice of grid aspect ratio, and the bulge in the reflected shock formed a smooth arc instead of a sharp cone. Changing the aspect ratio of the grid appears to be an effective way of eliminating the jetting at the axis; however, this approach is unsatisfactory from the standpoint of attempting to create numerical schemes that are grid independent. Therefore, this solution to the axis problem should be considered only as a temporary fix until a better method can be found. Ultimately, experimental data may be required to resolve this issue.

Another way that was suggested in Ref. 3 to alleviate the jetting problem was to compute the solution using only first-order spatial accuracy. This approach essentially causes the numerical scheme to become more dissipative, which in turn mitigates the jetting effect. Using a first-order formulation does have some serious consequences, however. Two solutions are compared in Fig. 6 (top and bottom), each on the same $\Delta x{:}\Delta y = 1{:}3$ grid. The first solution employed first-order spatial accuracy, whereas the second used second-order accuracy. This comparison showed that as the reflected shock continued to propagate up the driven tube, the dissipative, first-order scheme lost any trace of the vortex structure, whereas the second-order solution clearly showed that the vortex structure remained. Therefore, it was clear that the study of this type of transient flow must be conducted using at least second-order spatial accuracy.

Another possible source of error at the axis may be the axis boundary conditions. To determine the effects of the symmetry boundary conditions on the solutions, a comparison was made with a solution where the entire plane was included in the computational domain (instead of just half of a plane). In this way the symmetry line was no longer on a boundary. This exercise was completed for both an axisymmetric and a two-dimensional formulation. The resulting axisymmetric flowfield solutions showed only very slight differences between the half-plane and whole plane computations. The two-dimensional cases also showed negligible differences. Whether the grid was clustered or coarsened at the axis, eliminating the axis boundary conditions did not change the result.

Geometric Effects

The effects of changing the geometry in the driven-tube/nozzle interface region were examined, and several parameters were studied: 1) changing the throat size, 2) changing the shape of the juncture between the two sections, and 3) changing the shape of the endwall of the driven tube.

The area ratios of the nozzle throats examined were $A/A^* = 100$, 190, and 570. Note that for these area ratios A is the exit area of the Ames 16 in. shock tunnel nozzle; however, only a small portion of the nozzle flow was computed. The $A/A^* = 190$ throat was actually used in the facility. The other two area ratios were chosen to bracket the 190 throat size. For this portion of the study, all flows were computed with an axisymmetric formulation. Temperature contours for the three throat sizes at $t = 120$ μs are shown in Figs. 7a–7c. A comparison of the temperature contours indicates that, although the flows within the nozzle sections were different for each case (in particular, the shock interactions in the subsonic portion of the nozzle were intensified by the smaller throats), the vortex structures in the driven tube were nearly identical. This suggests that the formation of the vortex system in the driven tube is not strongly dependent on throat size.

Three changes were made to the geometry at the endwall of the driven tube. These changes, shown in Figs. 8a–8c, increased the diameter of the aperture in the endwall by 35% (Fig. 8a), rounded the juncture between the nozzle and the endwall (Fig. 8b), and tapered the endwall of the driven tube (Fig. 8c). The throat size was held fixed to the $A/A^* = 190$ size.

Increasing the diameter of the aperture initially caused a slight increase in the deformation of the reflected shock. However, by 120 μs after shock reflection, the solution looked very similar to the original $A/A^* = 190$ solution shown in Fig. 7b. Rounding the juncture between the nozzle and the endwall again caused the reflected shock to be more distorted, especially near the axis where the bulging effect was increased. Again, however, by 120 μs the solution looked very similar to the original solution.

The last geometric change that was examined was altering the shape of the endwall of the driven tube. The endwall was tapered from the juncture so that it was no longer vertical, and again the juncture between the two sections was rounded. This flowfield looked considerably different than those examined earlier. There were strong, transient shocks in both the subsonic and supersonic portions of the nozzle that were not seen in the other cases. The central vortex was significantly larger than in the other cases, causing the reflected shock to bulge out more. However, once again, by

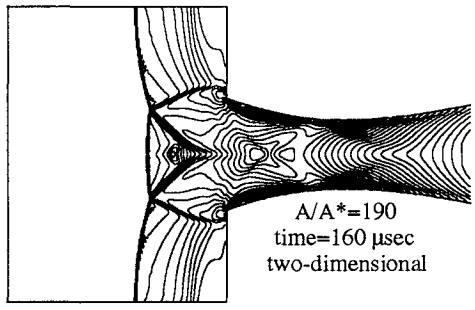

Fig. 9 Transient shock reflection solution for a two-dimension flowfield.

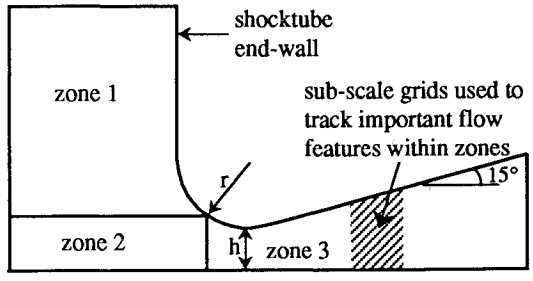

Fig. 10 Nozzle geometry and schematic of the zonal grids used for the transient nozzle flow computations.

120 μs the overall structure in the reflected shock region looked like the case with the original geometry. The important exception was that at t = 120 μs the reflected shock system (reflected shock and vortices) had traveled farther up the driven tube than for the other cases. The reason this occurred was because the endwall was angled into the driven tube, causing the primary shock to reflect sooner.

It is important to note that all of the previous calculations assumed that the flow was inviscid. Therefore, the viscous effects that may occur due to geometric changes were not examined. Viscous effects may not be insignificant, and further study is required to determine their importance to this problem.

For the bulging of the reflected shock to cause premature contamination of the test gas, it would have to persist long enough to interact with the contact discontinuity (CD). The original A/A^* = 190 case was continued until t = 400 μs, and it was found that the bulge did diminish as the reflected shock continued to propagate up the driven tube. Eventually, the reflected shock became almost planar. Therefore, the likelihood of premature mixing will depend on how much time elapses before the CD and the reflected shock interact. Note that, for this study, the driven tube walls were assumed to be inviscid; therefore, the effects of shock-wave/boundary-layer interactions, which could also cause premature contamination, were not examined.

The possibility that the bulge in the reflected shock was a purely axisymmetric phenomenon was also examined. Temperature contours for a two-dimensional calculation using the original A/A^* = 190 geometry at t = 160 μs are shown in Fig. 9. For the two-dimensional cases, the centerline vortex does not form; furthermore, the portion of the reflected shock near the centerline actually lags behind the rest of the shock. This type of two-dimensional flow structure has also been observed experimentally.[8]

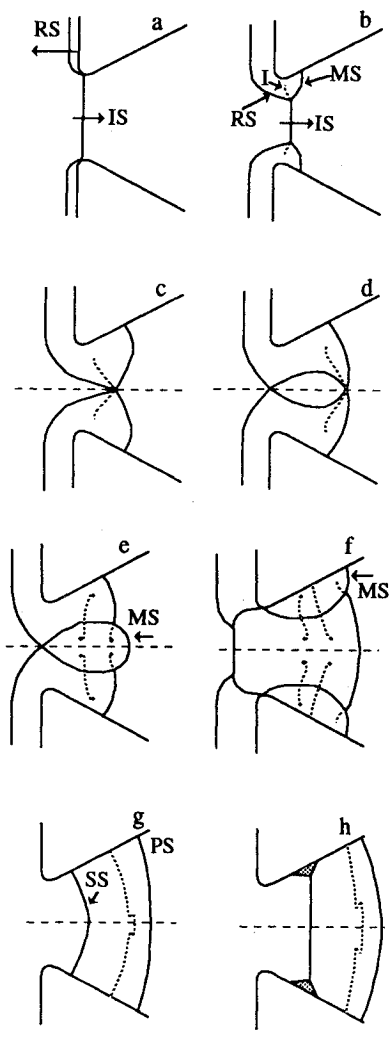

Fig. 11 Schematic of the transient nozzle flow development: I—interface, IS—incident shock, MS—Mach stem, PS—primary shock, RS—reflected shock, and SS—secondary shock.

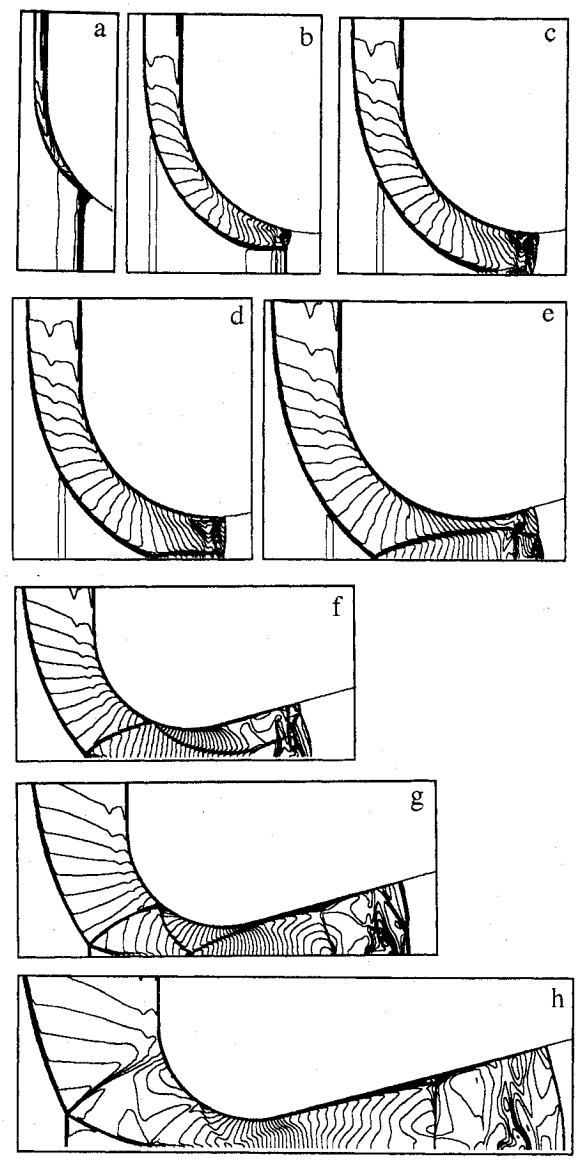

Fig. 12 Temperature contours of the computational results corresponding to the flow schematic presented in Fig. 11a–11h. The contours are drawn at 20 deg (K) intervals. Note that only half planes are shown.

Transient Nozzle Flow Simulation

Setup

The nozzle flow examined computationally in this study was originally examined experimentally by Amann and Reichenbach[8] and Amann.[9,10] The nozzle was two dimensional, and the experimental arrangement used side plates in the supply tube to reduce viscous effects upstream of the nozzle. The test was initiated with a Mach 3.0 shock in air upstream of a nozzle with a 15-deg semidivergence angle. The shock propagated into stagnant gas with T = 293 K and p = 6.3 kPa. The nozzle had a rounded inlet with a radius of r = 10 mm and a throat half-height of h = 3 mm (see Fig. 10).

The numerical study was initialized with a planar, M_s = 3 shock just upstream of the shock tube exit. The shock tube section was calculated with slip wall boundary conditions. The walls of the

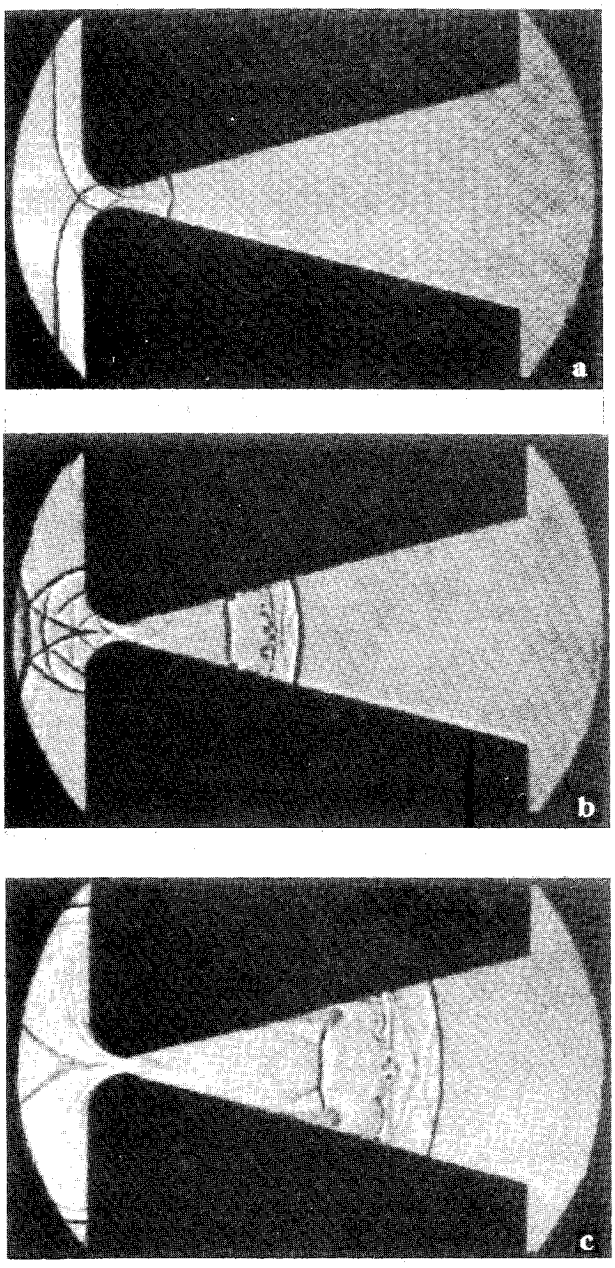

Fig. 13 Shadowgraphs of the starting process of a reflection nozzle with a rounded inlet, $M_s = 3$. Time between pictures about 35 and 50 μs.

nozzle, however, were calculated with no-slip boundary conditions since viscous interactions in the nozzle produced some of the dominant features in the flowfield. This nozzle flow was also examined computationally by Prodromou and Hillier[11]; however, those calculations were entirely inviscid.

The computational grid was constructed with three zones, as shown in Fig. 10, and subscale, high-resolution grids were used to track important flow features. This method was discussed in the numerical methods section. In all, two subscale grids were used: one to track the primary shock and contact surfaces and a second to track the secondary shock. These flow features are discussed in more detail later. The grid sizes were as follows: zone 1 = (250 × 140), zone 2 = (250 × 60), zone 3 = (840 × 60). The subscale grids were each 280 × 120 and were seven times as fine as the coarse grid in the axial direction and twice as fine in the radial direction. The subscale grids were used only in zone 3.

Results

The general evolution of the wave system within the nozzle is shown in Figs. 11a–11h. The computational equivalents of Figs. 11a–11h are shown by way of temperature contours in Figs. 12a–12h. All features shown in Figs 11a–11h, which are described later, were observed in the computational results. Note that the temperature contours were drawn at even 20 K intervals.

The nozzle flow develops as follows. Initially the incident shock enters the nozzle, and a regular reflection occurs at the nozzle walls (Fig. 11a). However, since the angle of incidence of the entering shock wave changes constantly, the conditions necessary for a regular reflection quickly break down and a Mach reflection develops (Fig. 11b). A contact surface (or interface) is associated with each Mach reflection. The Mach reflection consists of a Mach stem, the reflected shock, and an incident shock. These three features meet at the triple point. As the flow continues to develop, the triple point approaches the symmetry plane (Fig. 11c). When the triple point meets the symmetry plane, a regular reflection of the Mach stem (which must now be considered to be another incident shock) occurs (Fig. 11d). Again the conditions necessary for a regular reflection quickly break down, and another Mach reflection (including the associated contact surface) develops on either side of the symmetry plane (Fig. 11e). The newly formed triple point then travels toward the nozzle wall, setting the stage for the forma-

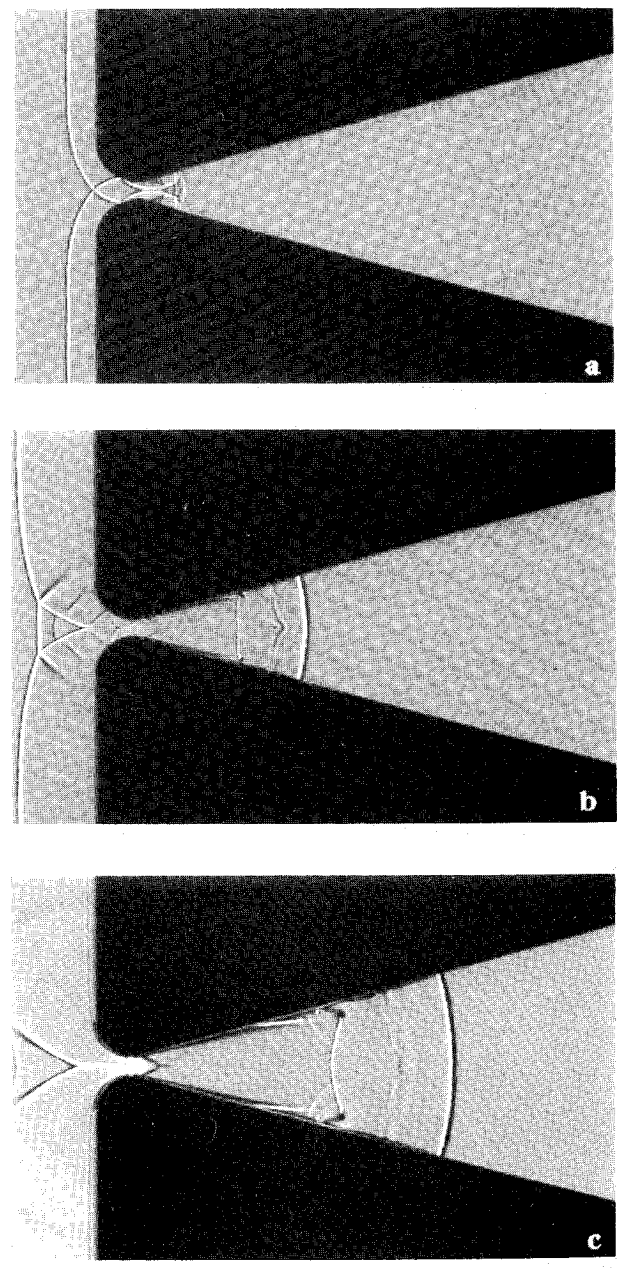

Fig. 14 Shadowgraphs constructed from the computational flowfield. Time between pictures about 35 and 50 μs.

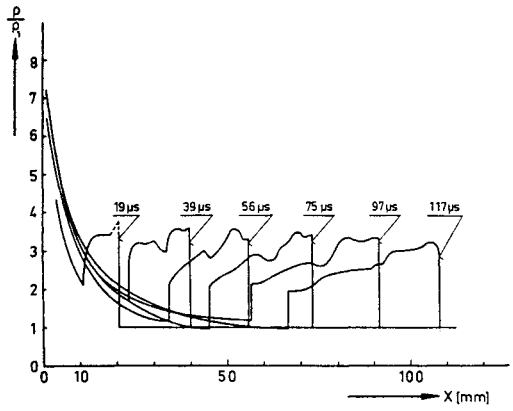

Fig. 15a The density on the nozzle axis at six stages in the starting process. Evaluated from interferograms.

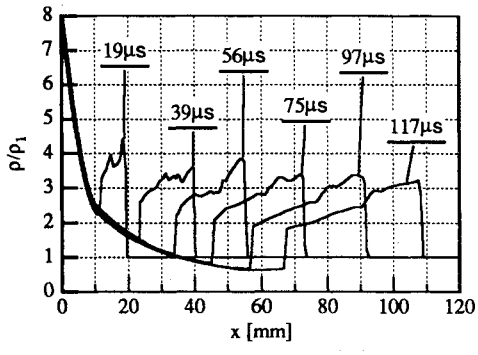

Fig. 15b The density on the nozzle axis at six stages in the starting process. Computational results.

tion of yet another Mach reflection (Fig. 11f). As the flow continues to develop, a secondary shock wave is formed that is facing upstream but being swept downstream (Fig. 11g). This secondary shock causes the boundary layer along the nozzle walls to separate (Fig. 11h).[8] It is interesting to note that the interaction of the secondary shock and the nozzle wall boundary layer very closely resembles the shock-wave/boundary-layer interaction problem associated with the propagation of a reflected shock in the driven tube of a shock tunnel as discussed in Ref. 12.

A series of experimental shadowgraphs (Figs. 13a–13c) and synthetic shadowgraphs[7] generated from the computed solutions (Figs. 14a–14c) demonstrate how the flow develops. The comparison shows that initially the shock systems and the contact surfaces were captured very well by the computations. However, as the flow progressed, the resolution of the contact surfaces began to degrade. Capturing contact surfaces using CFD can be difficult since the numerical methods are tuned to capture discontinuities like shock waves with converging characteristics on either side of the discontinuity. Also, numerical and viscous dissipation tends to dissipate the contact surfaces. Ways of improving the resolution of the contact surfaces obviously require further study. It should be noted, however, that the ability to discern the contact surfaces was greatly improved by tracking them with a higher resolution grid. Solutions computed using only the coarse grids showed that the contact surfaces were all but nonexistent in the latter portion of the nozzle.

The boundary-layer separation (Fig. 13b) was captured well by the computations (Fig. 14b). However, as the secondary shock moved downstream, the CFD solutions predicted that this shock became curved (Fig. 14c) instead of remaining mostly planar as was shown in the experimental shadowgraph (Fig. 13c). The reason for this is not fully understood; however, one possible cause may be that the boundary layer upstream of the secondary shock was not modeled precisely enough, causing the shock-wave/boundary-layer interaction to be different than in the experiment. There is some indication in the experimental shadowgraphs that the separated region may have been turbulent. The calculations assumed that the entire flowfield was laminar; therefore, any turbulent effects were not captured.

The density along the nozzle axis at six different times during the starting process was discerned from interferograms by Amann and Reichenbach (Fig. 15a).[8] The density profiles from the CFD solutions at the same times are shown in Fig. 15b. The computations agree very well with the experimental results. In particular the locations of the primary and secondary shocks were captured well throughout the simulation, indicating that the shock speeds were predicted accurately. Also, the features within each profile were captured well.

Conclusions

It was found that refining the grid in the radial direction such that $\Delta x{:}\Delta y \geq 1$ produced a nonphysical jetting behavior along the axis. A partial explanation was given, and changing the grid aspect ratio such that $\Delta x{:}\Delta y \geq 3$ was presented as a temporary solution to the jetting problem. Better ways to solve this problem are currently being studied. Spatially first-order-accurate solutions were found to be too dissipative to resolve the vortex structure in the driven tube.

Several geometric changes were made to both the nozzle section and the driven tube to determine their effects on the flowfield. It was found that increasing the diameter of the aperture in the endwall of the driven tube and rounding the juncture between the nozzle and driven sections both initially caused changes in the reflected shock region; however, by $t = 120$ μs after shock reflection, the reflected shock region for both cases looked the same as a case with a smaller aperture and a sharp interface between the sections. It was found that tapering the endwall of the driven tube initially caused the reflected shock to bulge more at the centerline; however, the increase in the bulge was not observed at later times ($t = 120$ μs). In all cases the reflected shock becomes almost planar by $t = 400$ μs after shock reflection. Overall, the geometric changes did not have a significant effect on the bulge in the reflected shock. The calculations assumed inviscid flow, and it was determined that further study was required to examine viscous effects that may occur due to geometric changes.

Two-dimensional flow solutions showed that no vortex existed in the driven tube, and the reflected shock near the centerline lagged behind the rest of the shock instead of protruding ahead of it as was seen in the axisymmetric formulation. The two-dimensional results agreed with experimental data.

The transient flow in a shock tube nozzle was calculated, and the results, including shock speed and overall flow structure, compared well with experimental results. The CFD solutions incorporated a grid-tracking technique where transient flow features of interest were tracked by high-resolution grids. This technique greatly improved the accuracy of the CFD solutions.

Acknowledgments

Support for Susan Tokarcik-Polsky was provided by NASA Grant NCC2-420. Support for Jean-Luc Cambier was provided by NASA Grant NCC2-487.

References

[1]Gaydon, A. G., and Hurle, I. R., "The Shock Tube in High-Temperature Chemical Physics," Reinhold, New York, 1963.

[2]Harten, A., "High Resolution Schemes for Hyperbolic Conservation Laws," *Journal of Computational Physics*, Vol. 49, No. 3, 1983, pp. 357–393.

[3]Cambier, J.-L., Tokarcik, S., and Prabhu, D., "Numerical Simulation of Unsteady Flow in a Hypersonic Shock Tunnel Facility," AIAA Paper 92-4029, July 1992.

[4]Jacobs, P. A., "Simulation of Transient Flow in a Shock Tunnel and a High Mach Number Nozzle," NASA CR-87606, July 1991.

[5]Mandella, M., "Experimental and Analytical Studies of Compressible Vortices," Ph.D. Dissertation, Dept. of Aeronautics and Astronautics,

Stanford Univ., Stanford, CA, 1987.

[6]Mandella, M., and Bershader, D., "Quantitative Study of Compressible Vortices: Generation, Structure and Interaction with Airfoils," AIAA Paper 87-0328, Jan. 1987.

[7]Yates, L. A., "Images Constructed from Computed Flowfields," AIAA Paper 92-4030, July 1992.

[8]Amann, H. O., and Reichenbach, H., "Unsteady Flow Phenomena in Shock Tube Nozzles," *Recent Developments in Shock Tube Research*, edited by D. Bershader and W. Griffth, Stanford Univ. Press, Stanford, CA, 1973, pp. 96–112.

[9]Amann, H. O., "Experimental Study of the Starting Process in a Reflection Nozzle," *Physics of Fluids*, Vol. 12, No. 5, 1969, pp. 150–153.

[10]Amann, H. O., " Vorgän beim Start einer ebenen Reflexionsdüse," *Zeitschrift für Flugwissenschaften*, Vol. 19, Oct. 1971, pp. 393–406.

[11]Prodromou, P., and Hillier, R., "Computation of Unsteady Nozzle Flows," *Shock Waves Proceedings* (Sendai, Japan) edited by K. Takayama, Vol. II, Springer-Verlag, Heidelberg, Germany, 1992, pp. 1113–1118.

[12]Wilson, G., Sharma, S., and Gillespie, W., "Time-Dependent Simulations of Reflected-Shock/Boundary Layer Interaction," AIAA Paper 93-0480, Jan. 1993.

Tactical Missile Aerodynamics: General Topics

Michael J. Hemsch, editor

This volume contains updated versions of three chapters from the first edition and six new chapters covering such topics as a history of missiles, system design, radar observables, unsteady flows, and store carriage and separation. More than 500 figures and five color plates support the text.

Contents include: Historical Review of Tactical Missile Airframe Developments; Aerodynamic Considerations for Autopilot Design; Radar Observables; Visualization of High-Angle-of-Attack Flow Phenomena; Low Aspect Ratio Wings at High Angles of Attack Inlets; Waveriders, and more.

1992, 700 pp, illus, Hardback
ISBN 1-56347-015-2
AIAA Members $64.95
Nonmembers $79.95
Order #: V-141(945)

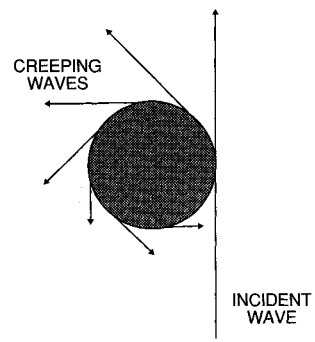

Save when you buy the complete set:
AIAA Members $120
Nonmembers $145
Order #: V-141/142(945)

Tactical Missile Aerodynamics: Prediction Methodology

Michael R. Mendenhall, editor

This book contains updated versions of nine chapters from the first edition and new chapters on drag prediction, component build-up methods, Euler methods, and Navier-Stokes solvers. Special attention is paid to nonlinear flow phenomena and unconventional airframe shapes. Eight color plates and more than 540 figures are included.

Contents include: Tactical Missile Drag; Drag Prediction Methods for Axisymmetric Missile Bodies; Introduction to the Aerodynamic Heating Analysis of Supersonic Missiles; Component Build-Up Method for Engineering Analysis of Missiles at Low-to-High Angles of Attack, and more.

1992, 700 pp, illus, Hardback
ISBN 1-56347-016-0
AIAA Members $64.95
Nonmembers $79.95
Order #: V-142(945)

Place your order today! Call 1-800/682-AIAA

AIAA
American Institute of Aeronautics and Astronautics
Publications Customer Service, 9 Jay Gould Ct., P.O. Box 753, Waldorf, MD 20604
FAX 301/843-0159 Phone 1-800/682-2422 9 a.m. - 5 p.m. Eastern

Sales Tax: CA residents, 8.25%; DC, 6%. For shipping and handling add $4.75 for 1-4 books (call for rates for higher quantities). Orders under $100.00 must be prepaid. Foreign orders must be prepaid and include a $20.00 postal surcharge. Please allow 4 weeks for delivery. Prices are subject to change without notice. Returns will be accepted within 30 days. Non-U.S. residents are responsible for payment of any taxes required by their government.